A Multi-LED Dome Bulb Prototype for Dense Visible Light Communication Networks

Pooya Nabavi[1,2,†], Sajad Saghaye-Polkoo[2,3,†], Murat Yuksel[1,2] , and Christopher Kyle Renshaw[1,2,3]
[1]Electrical and Computer Engineering, University of Central Florida, Orlando, FL USA 32816
[2]CREOL, The College of Optics and Photonics, University of Central Florida, Orlando, FL USA 32816
[3]Departments of Physics, University of Central Florida, Orlando, FL USA 32816
pooya.nabavi@knights.ucf.edu, sajad.saghaie@knights.ucf.edu, murat.yuksel@ucf.edu, krenshaw@creol.ucf.edu
[†]These authors contributed equally to this article.

***Abstract*—In this paper, we employ imaging-based beam-steering to enable multi-datastream visible light communication networks serving dense Internet-of-Things (IoT) deployments. We demonstrate a "dome bulb" transmitter that consists of a multi-LED array with a dome-shaped lens to separate each LED's beam for better spatial reuse. Each LED has a Lambertian irradiance distribution that is collected efficiently and directed along a particular line-of-sight using a wide field-of-view lens system. At focus, the image of the LED array is projected to a distant conjugate plane, and LED beam divergence is minimized to the geometric limit. This improves spatial reuse by minimizing interference between adjacent beams but results in spotty illumination due to gaps between LEDs in the array. Moderate defocusing blurs the beams to increase illumination uniformity at the expense of increased cross-channel interference. We present a model for the bulb that correlates to the experimental results and quantify the performance of the prototype for dense IoT networks.**

***Index Terms*—Visible Light Communications, Illumination Uniformity, Multi-Datastream Optical Wireless Communication Networks.**

I. Introduction

The modern information age is characterized by rapid growth in connected devices and an ever-increasing demand for data volume. Connectivity has expanded beyond dedicated communication devices to any "thing" around us giving rise to the Internet-of-Things (IoT). In the IoT landscape, a watch tells more than time, a doorbell more than rings, a refrigerator more than cools as they are connected to provide convenience features that we generically describe as "smart". The continued growth in the density of these IoT devices and the data bandwidth requires new communication technologies beyond legacy radio frequency (RF)-based networks, such as Wi-Fi [1]. Current 5G technologies are limited to data-com service providers, but may eventually mature to consumer devices that provide affordable bandwidth relief to end users. Beyond 5G, optical wireless communications (OWC) promises extreme bandwidths capable of >1 Tbps to meet the most demanding mobile data needs of the future [1]. OWC presents unique challenges and opportunities associated with optical domain carrier frequencies that are >1000x larger than 5G frequencies and, in principle, offer a commensurate increase in bandwidth. Challenges include 1) managing the line-of-sight (LOS) nature of OWC datalinks, 2) implementing efficient and highly directional point-to-point links, and 3) implementing affordable architectures that take advantage of the extreme bandwidth available. Opportunities include 1) long-range, high-bandwidth datalinks without hardwired fiber-optic infrastructure, 2) secure links that are hard to eavesdrop, 3) robust links immune to jamming and congestion in the limited RF spectrum, and 4) spectrum reuse via spatial multiplexing.

A major branch of visible light communications (VLC) research seeks to reuse light fixtures or "luminaires" for wireless networking over short distances. Modulation of luminaires faster than eye response allows data transmission while still providing stable illumination [1], [2]. Wide-angle (i.e., diffuse) emission from luminaires provides an omnidirectional signal observable by any receiver in the luminaires's illumination pattern but this poses a limit to the bandwidth available in the simplest VLC downlink architecture [3]. Phosphorescent light-emitting diode (LED) bulbs are typically limited to a few tens of MHz bandwidth by the relaxation time of the

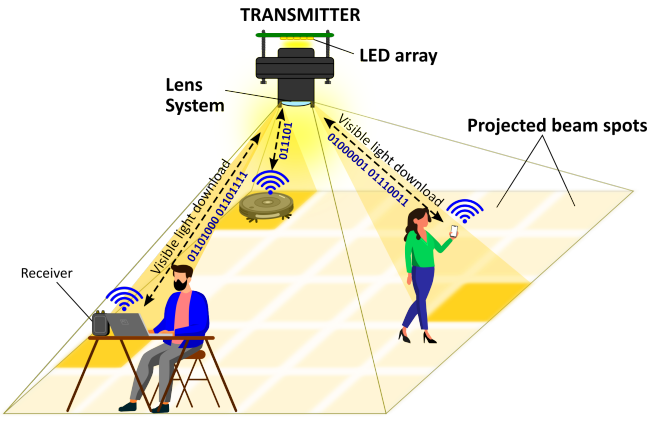

Fig. 1. Multi-datastream VLC Architecture Using Dome Bulb: Each LED on the bulb illuminates a certain area in the room. IoT receivers can simultaneously download from their corresponding LEDs on the bulb, and upload via legacy RF.

This work was supported in part by Air Force Office of Scientific Research; U.S. Air Force (FA8650-16-D-5408) and U.S. National Science Foundation award 2120421.

The authors would like to thank Photon Engineering, LLC for their invaluable licensing assistance with FRED Optical Engineering software.

down-converting phosphors and the electrical impedance of the diodes [4]–[9]. Their speed can be increased toward the GHz regime by removing the broadband phosphor and combining narrowband red, green, and blue LEDs to generate white light limited by the spontaneous emission rate of the LED [10]. Likewise, utilizing stimulated emission from semiconductor lasers can exceed this limit to push the bandwidth beyond 1 GHz [11], [12]. However, implementations that use narrowband sources tend to suffer from lighting quality, as they exhibit a low color rendering index (CRI) [13]. As a recent concept, multi-datastream VLC networks [14]–[16] can increase the aggregate bandwidth using multiple concurrent VLC download links to serve dense IoT deployments. We focus on this type of VLC networks and propose a novel component to improve them.

There are two critical goals for VLC systems using luminaires. The first is to provide fast and reliable data connectivity to compliment existing wireless communication technologies and meet the continued growth in demand for bandwidth. The second goal is to maintain high-quality lighting of the luminaires they replace; i.e., the lighting should be uniform spatially and spectrally while providing good CRI and power efficiency. The luminaire must also be cost effective and long-lived, ideally without moving parts. The ideal bulb would also be easy to install and would require a minimal number of fixtures and wiring per area of coverage.

We introduce a prototype luminaire design, specifically a bulb, that can meet this challenging combination of requirements. The bulb uses a dome-shaped lens structure to implement imaging-based beam steering (IBBS) which provides numerous, directional and spatially-multiplexed channels out of a single bulb [17], [18]. To provide multiple VLC download links simultaneously, our bulb uses a 25-LED array behind the lens structure to separate each LED's beam for spatial reuse. The LED array can serve as a generic programmable platform for establishing connectivity, tracking, and maintaining the link as users move in the room. The bulb effectively partitions its illumination into 25 zones (that is, channels or datalinks) that can be driven independently. This approach allows one bulb to illuminate and connect a large area, while increasing aggregate data throughput to numerous devices and minimizing interference. Using one bulb to serve many zones potentially reduces hardware and installation costs per area covered and/or data capacity. We utilize packaged, white LEDs with a broadband, down-converting phosphor and a 20 MHz bandwidth. Each LED is independently addressed with a DC bias for illumination and an AC bias in addition for data transmission to provide optical downlink channels that can be modulated separately. When not transmitting data, the LEDs stay on by emitting a DC signal. When an LED transmits data, a Bias Tee is used to superimpose a data-carrying AC current on top of the DC signal.

Fig. 1 illustrates an example scenario using our prototype bulb to illuminate a room while providing multiple simultaneous VLC download links to receivers distributed around the room. Each receiver may be a simple photodiode that collects the modulated signal independent of its angle-of-arrival or the detector orientation as long as it nominally faces up towards the ceiling. While such a receiver is sensitive to interference from other light sources, steady-state sources can be filtered electronically. The interference is then dominated by direct crosstalk between active channels from adjacent LEDs on the array and scattering of other channel emission. In this simple example, the uplink is done via RF technologies such as Wi-Fi.

We build and demonstrate a ceiling-mountable prototype of the bulb using 25 LEDs arranged in a planar array. We analyze the bulb in terms of illumination uniformity, Signal-to-Noise Ratio (SNR), and Signal-to-Interference-plus-Noise Ratio (SINR) provided to receivers in the room. Since the emission from each LED is projected to illuminate a particular zone of the room (as shown in Fig. 1), our bulb design also brings about the problem of spotty lighting. To develop insights into the trade-offs among these factors, we investigate the bulb's emission properties, such as uniformity, crosstalk, and SINR as a function of defocus and receiver position within the irradiance map. Furthermore, we simulate and extract the SINR map and illumination uniformity resembling the actual implementation and then find the optimized operation point considering the trade-off between illumination uniformity and SINR (SNR) quantitatively.

Our main contributions include:

- A multi-LED dome-shaped bulb design that allows multiple VLC downlinks for settings where dense deployment of receivers is the norm.
- A thorough study of irradiance maps for the multi-LED bulb system while varying defocus amount.
- Analysis of the tradeoff between SINR and lighting uniformity in the dome bulb.
- A prototype implementation of the dome bulb system.
- Empirical characterization of the VLC channel being offered by the dome bulb.

The rest of the paper is organized as follows: In Section III, we introduce a theoretical description of an IBBS-based VLC system. In Section IV, we describe the experimental methods used to make the prototype transmitter and characterize its optical and communication properties. In Section V, we provide the experimental results of the prototype and evaluate the trade-off between illumination uniformity versus channel crosstalk, and discuss methods to further improve VLC systems using the IBBS approach. Finally, we summarize our work with concluding remarks and future works in Section VI and VII.

II. Related Work

Separation of transmitter sources in a multi-datastream VLC network received sizable attention recently, for the purpose of increasing aggregate bandwidth. Driving each color separately in an assembly of narrowband sources was explored to further increase the bandwidth via wavelength division multiplexing [19]. Alternatively, bandwidth can be increased by using multiple bulbs distributed around a room where each bulb addresses part of a room, as shown by Alshaer *et al.* [14]. This spatial multiplexing takes advantage of the LOS characteristic of optical links. In a similar vein, Little *et al.*

[20] examined several aspects of user interaction, including interactions between multiple users, mobility and orientation of the device, and user traffic in such multi-cell LiFi networks. The purpose of their unique multi-cell lighting testbed was to analyze and optimize LiFi systems. However, scaling through increasing the number of VLC cells is limited by crosstalk between adjacent bulbs along with increasing hardware and installation costs.

Recent reports have utilized pixelated emitter arrays of narrowband, infrared, or low-brightness sources to generate and steer OWC beams without providing general illumination. Toyoshima *et al.* [21], [22] used a VCSEL array and CCD to demonstrate this method of spatial filtering for bi-directional links. Koonen *et al.* [1] showed that a bundle of optical fibers could be arranged to serve as a pixelated emitter array. In that work, wavelength-based routing was provided using an array waveguide grating to route datalinks to invididual fibers in the array. While the narrow and near-infrared spectrums are well suited for communications, they are insufficient for illumination. Chang *et al.* [23] used integrated photonics to route signals to an array of outcouplers in combination with a metalens to steer each pixel into unique directions. Coupled with a lens, this produced wavelength-steerable infrared beams covering a 17degree FOV. In the visible spectrum, a pixelated MIMO system was proposed in [24] using a lens to project a transmit array to infinity and an infinity-focused camera (i.e., receiver) to image multiple pixels from the transmit array. By collecting multiple pixels into a single receiver FOV, spatially-encoded data like a QR-codes could be viewed. This allows increasing the capacity of the link if each pixel can be modulated at high speeds. However, neither Tx or Rx hardware is readily available to do this in practice; a high-speed camera with ≈10 KHz frame rates and a 1000 sub-channels only yields a 10 Mbps link comparable to a single phosphorescent LED. In 1991, Short *et al.* [25] demonstrated a similar solution for low data-rate links using a high speed camera for the receiver array but employing a single laser translated around the focal plane of a transmit lens rather than using a pixelated emitter array. None of these prior works provided illumination alongside their pixel-steered datalinks out of a single bulb.

Our work differs from these prior studies as it demonstrates a novel VLC transmitter, or bulb, that (i) employs a dome-shaped lens system in front of an LED array to provide multiple, spatially-filtered datastreams and (ii) addresses the illumination uniformity by tuning the defocus amount. The bulb design provides an effective means to dual-purpose luminaires and implement VLC systems wherein all beam-forming and control is performed in the stationary bulb. Spatial filtering provided by the bulb supports numerous device connections at full bandwidth while minimizing inter-channel interference; and the design facilitates covering a large area, densely populated with devices out of a single aperture. Passive steering via IBBS accomplishes this without moving parts to control the beam direction. Utilization of high-brightness, broad-spectrum LEDs yields sufficient luminous flux for lighting purposes and promises good color-rendering, power efficiency, and lifetime.

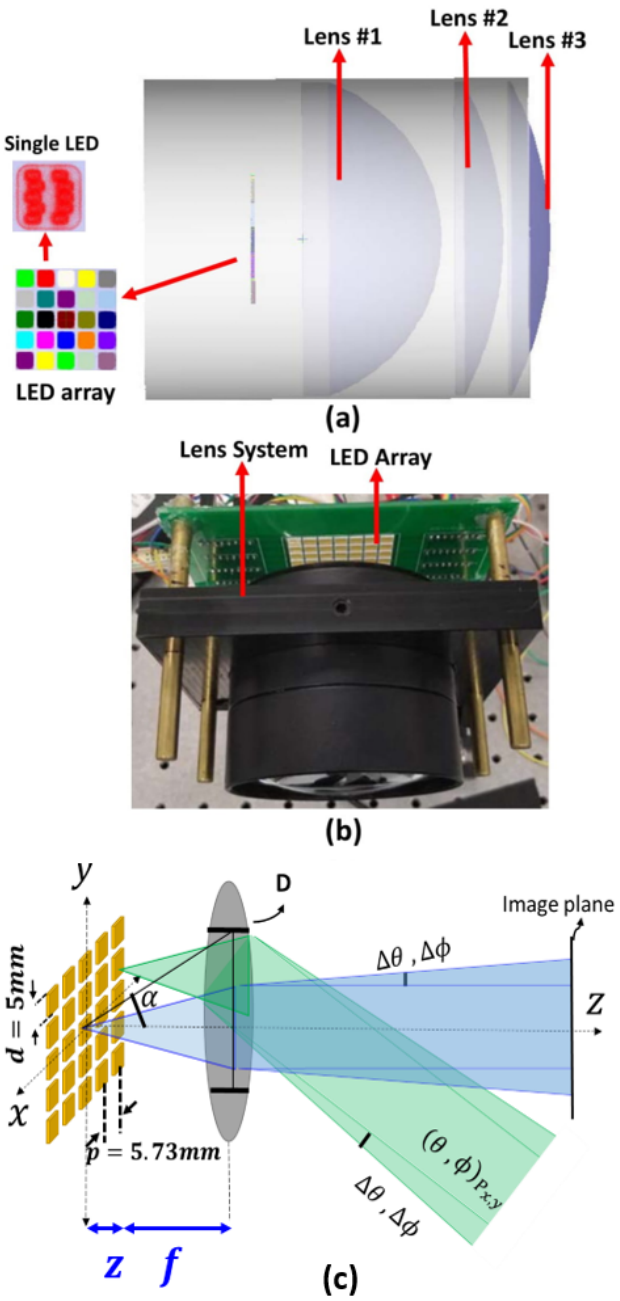

Fig. 2. Prototype Imaging-Based Beam Steering (IBBS) VLC Transmitter; (a) Schematic showing the 5×5 LED array at the focal plane of a 3-element lens, (b) Photograph of the prototype, (c) Illustration of the spatial mapping from the LED array into line-of-sight (LOS) directions; position of the LED array z is increasing away from the lens starting at with z=0 at the front focal plane of the lens (i.e., prime focus).

III. Theory

An ideal VLC system would provide a large number of independent, simultaneous, high-speed, and bi-directional datalinks covering a large room with zero crosstalk between datalinks. To replace conventional luminaires, it should also provide high quality and uniform lighting, have a long lifetime and be inexpensive. Our recent work on IBBS provides a scalable solution to enable ideal VLC systems as it can provide numerous datalinks out of a single aperture using low-cost

components without costly mechanical or phase-based steering [17]. As illustrated in Fig. 2(a), an IBBS transmitter (Tx) uses a planar array of independently driven sources positioned at the front focal plane of an imaging optic. Emission from each source is collected, collimated and steered into a unique LOS direction based on its position in the focal plane. In a rectilinear lens with low distortion, the mapping from focal plane position to LOS is accurately described by first-order optics as

$$(\theta_m, \phi_n) = \left(\tan^{-1}\left(\frac{x_m}{f}\right), \tan^{-1}\left(\frac{y_n}{f}\right)\right) \qquad (1)$$

where f is the lens focal length, (x_m, y_n) are the coordinates of the center of the emitter in the m^{th} column and n^{th} row while (θ_m, ϕ_n) are the conjugate LOS directions. The field-of-view (FOV) coverage of an $M \times N$ array is $FOV = \tan^{-1}(pM/f)$ in the x-axis where p is the column pitch; and a similar expression follows for the y-axis. This gives the angular center-to-center distance between emission from LEDs at opposite edges of the array and neglects their beam width. With the source array positioned precisely at the lens front focal plane, emission from each source is passively steered by the lens into its infinite conjugate direction. This could be described as Fourier Transform Beam-Steering when the array is constrained to the Fourier (i.e., focal) plane, however, we show that displacing the array from prime focus gives useful control over beam divergence. In this context, the term IBBS is more appropriate when we consider imaging to finite conjugates as well.

In principle, the same architecture could be used for IBBS receivers (Rx) by replacing the sources and drive electronics with high-speed photodetectors and signal processing. The Rx and Tx could share the same aperture employing a beam-splitter to separate the Rx/Tx paths in the space leading up to the lens - we will refer to this as "image" space whereas beams propagate between distant transceivers in "object" space. In the remainder of this paper, we confine our discussion and prototype demonstration to an IBBS Tx. While there is some symmetry between Tx and Rx, the Tx side presents a particularly challenging set of requirements for VLC implementation as it must meet requirements for both illumination and communication [26]. Likewise, some VLC architectures consider hybrid networks that only use optical domain for downlink (i.e., Tx from the hub to end-use devices) while RF is used for uplink in order to simplify the hardware requirements at end-use devices [27].

TABLE I
OPTICAL SYSTEM PARAMETERS

surface	Radius (mm)	Thickness (mm)
Object (LED Array)	infinity	9 + z (defocus)
L1 Front	infinity	32.62
L1 Back	-38.76	3
L2 Front	infinity	11.45
L2 Back	-77.52	1
L3 Front	infinity	11.45
L3 Back	-77.52	2000
Image (Floor)	infinity	

All glass is BK7, EFL is 41.56(mm), Entrance pupil diameter is 106(mm), Object Space NA is 0.66

It is important to recognize some characteristic features of this beam-steering solution: 1) steering is restricted to discrete LOSs with one LOS per source, 2) steering a data stream is realized by selecting which source to use for the stream, and 3) a virtually unlimited number of sources could be steered out of a single aperture. The last characteristic arises from the non-interacting nature of photons combined with the passive optical steering mechanism in IBBS but, in practice, the number of independently driven sources is limited by the area available for sources and drive circuitry. An ideal IBBS source array would contain a large number of high-speed emitters packed at high-density covering a large area (comparable to f^2, for example) because this spatial arrangement determines the number of independent channels, link bandwidth, FOV coverage and system resolution. However, realizing this combination is difficult and such ideal sources are not commercially available today. Similar source technologies have been demonstrated for infrared communications and LIDAR imaging using VCSELs [28], fiber bundles [1], and photonic integrated circuits [17]. For VLC, each emitter must also provide good color quality (i.e., white light with a desired color temperature and high CRI) and sufficient brightness into its portion of the FOV, i.e., the instantaneous FOV, iFOV.

A well-corrected lens can yield low beam divergence ($\Delta\theta$) even from wide angle sources such as LEDs, VCSELs or compact gratings. In [18], we demonstrated few mrad beam divergence from a non-directional (i.e., Lambertian) organic LED source array. A lens with diffraction limited performance yields spot size given by the Airy disk diameter $b = 2.44\lambda F$, where $F = f/D$ is the lens F-number and D is its entrance pupil diameter. When b is smaller than the emissive width of the source (d) so that $b < d$, beam divergence is limited geometrically by $\Delta\theta = \tan^{-1}(d/f)$; thus longer focal length and smaller source reduce beam divergence. Lens aberrations could further degrade beam collimation but well-corrected lenses are readily available for a wide-range of focal lengths and spectral bands.

Optical efficiency (η_{opt}) of an IBBS Tx can be quantified as the fraction of radiant flux contained in the collimated beam compared to the total flux leaving the source. This efficiency can be high if the angular emission of the source lies within the acceptance cone of the lens. On-axis the acceptance cone of the lens is given by the half-angle (α) as

$$\alpha = \tan^{-1}\left(\frac{D}{f}\right) = \tan^{-1}\left(\frac{1}{2F}\right) = \sin^{-1}\left(\frac{NA}{n}\right) \qquad (2)$$

where NA is the numerical aperture and n is the index of image space - typically air with $n = 1$ in this application. If source emission lies within α, light can couple efficiently into the entrance pupil and coupling can approach unity limited by reflection, absorption losses and vignetting propagating through the lens. The efficiency of coupling non-directional sources such as Lambertian emitters can be calculated for a

point-source on-axis as

$$\eta_{opt} = \frac{\int_0^{\alpha}\int_0^{2\pi} g(\theta,\phi)\sin(\theta)\mathrm{d}\phi\mathrm{d}\theta}{\int_0^{\pi/2}\int_0^{2\pi} g(\theta,\phi)\sin(\theta)\mathrm{d}\phi\mathrm{d}\theta} \quad (3)$$

where $g(\theta,\phi)$ is the radiant intensity of the source in W/sr, θ is the "elevation" angle from the emission axis, ϕ is the "azimuth" or rotation angle about the emission axis. The ϕ integrals span 0 to 2π in both the numerator and denominator. In the numerator, the θ integral includes all light collected by the lens - spanning 0 to the acceptance cone angle α from Eq. (2). The θ integral in the denominator includes all light emitted - spanning 0 to $\pi/2$. If the emission is rotationally symmetric where $g(\theta,\phi) = g(\theta)$ or even just separable $g(\theta,\phi) = g_\theta(\theta)g_\phi(\phi)$, the ϕ integrations cancel out. Furthermore, if the source is Lambertian with $g(\theta,\phi) = P_0\cos(\theta)$, then Eq. (3) reduces to $\eta_{opt} = P_0\sin^2(\alpha)$. Additional losses from propagation through the lens system can be minimized with anti-reflection coatings. Off-axis several lens characteristics could degrade η_{opt} including increase in effective F-number, large chief-ray skew angles and vignetting. Lens aberrations are also likely to be significant away from the optical axis.

When the IBBS lens is precisely focused, it will produce an image of the source array projected to an infinite conjugate distance. Additionally, this image will reproduce any dark spots on the source array caused by source gaps, resulting in spotty lighting with poor spatial uniformity. Gaps in the array can be minimized by using a monolithically integrated LED array fabricated on a single chip, but high-density integration of high-speed driver circuitry presents a challenge. To address illumination gaps, one could use a diffuser or deliberately defocus the lens to soften dark or bright spots and improve uniformity. However, this typically results in additional optical losses and/or increased crosstalk between adjacent channels. We evaluated both methods and discuss in detail how defocus can be used to find a balance between spatial uniformity and channel isolation; we briefly discuss the impact of a diffuser in Section V.

Spatial illumination uniformity (U) is quantified using the steady-state luminous flux density (i.e., illuminance) distribution as

$$U = \frac{\sqrt{\int_A \left[\frac{L^2 - <L>^2}{A}\right]\mathrm{d}x\mathrm{d}y}}{<L>} = \frac{\sqrt{\int_A \left[\frac{I^2 - <I>^2}{A}\right]\mathrm{d}x\mathrm{d}y}}{<I>} \quad (4)$$

where $L(x,y)$ is illuminance (notionally on the table or floor of an illuminated room), $< L >$ is the spatial average of L over the illuminated region of area A and the integral is evaluated over the same region. Thus U is the standard deviation normalized by the average illuminance; we consider $U < 10\%$ for good lighting of indoor environments [29], [30]. Proper characterization of lighting must consider L which weights the illumination by the eye spectral response to quantify the perceived brightness. Through normalization by $< L >$ this particular metric (U) allows the second equality cast in terms of irradiance $I(x,y)$ and its spatial average $< I >$. This is convenient because the communication aspect of VLC systems depend on I and the receiver's spectral response rather than L. Notably, this second equality holds true only if the illumination is spectrally uniform across the illuminated area; then $L(x,y) = CI(x,y)$ where C is the spectral overlap integral between the illumination and eye response which is a constant under these conditions.

crosstalk between (spatially) adjacent channels can be quantified using the overlap integral of the irradiance patterns of any two channels. Let channel (m,n) refer to the light beam transmitted from the LED on the m^{th} row and n^{th} column of the LED array. If channel (m,n) has an irradiance pattern $I_{m,n}(x,y)$ and channel (i,j) has a pattern $I_{i,j}(x,y)$ then the fractional overlap of $I_{i,j}(x,y)$ on $I_{m,n}(x,y)$ is:

$$X_{i,j}^{m,n} = \frac{\int\sqrt{I_{m,n}I_{i,j}}\mathrm{d}x\mathrm{d}y}{\int I_{m,n}\mathrm{d}x\mathrm{d}y}. \quad (5)$$

This is useful to characterize the degree of crosstalk at the system level, but in practice a receiver samples only a small portion of a channel(s) emission so that the amount of crosstalk received depends on the precise location of the receiver within the irradiance pattern of the VLC bulb.

Crosstalk into a receiver's aperture represents an interference that degrades the integrity of the intended signal. We adopt SINR as a measure of signal integrity in the presence of interference caused by crosstalk. The SINR for channel (m,n) is given by

$$SINR_{m,n}(x,y) = \frac{A_{Rx}I_{m,n}(x,y)}{P_{noise} + A_{Rx}I_{interference}} \quad (6)$$

where A_{Rx} is the receiver aperture, P_{noise} is the noise power and $I_{interference}$ is the irradiance at the receiver from any other communication channel due to crosstalk. A_{Rx} is assumed small so that the irradiance across its aperture can be considered constant, $I_{m,n}(x,y)$, depending on its (x,y) location. The noise power is given by $P_{noise} = \sigma_T^2 + \sigma_D^2 + \sigma_{BG}^2$ where $\sigma_T^2 = 4k_BTBF_n/R_L$ is the thermal noise power, $\sigma_D^2 = 2qBJ_DR_L$ is the shot-noise power from dark current, $\sigma_{BG}^2 = 2qBJ_{BG}R_L$ is the shot-noise power from steady-state background illumination [31]. Here, k_B is Boltzmann's constant, T is temperature, B is system bandwidth, F_n is a detector noise figure, R_L is the detector's load resistance, J_D is the detector dark current, $J_{BG} = RI_{BG}A_{Rx}$ is the photocurrent generated by steady-state background illumination, R is the spectrally-averaged detector responsivity, and I_{BG} is the steady-state background irradiance at the receiver aperture ignoring any modulated optical signals. The spectral average in R includes the LED emission and detector response spectra to yield the correct photocurrent given a broadband irradiance, I_{BG}, from the source. We disregard shot-noise fluctuations on intentionally modulated irradiance (i.e., interference arising from crosstalk) and simply count this power directly in the SINR metric; small (i.e., shot-noise) fluctuations on a large fluctuating (i.e., modulated) signal are not considered significant. Interference includes any direct coupling due to crosstalk between channels and is given by

$$I_{interference} = \sum_{i\neq m}\sum_{j\neq n}\Lambda_{i,j}I_{i,j}(x,y) \quad (7)$$

where $\Lambda_{i,j} = 1$ or 0 if channel (i,j) is actively transmitting data or not. We disregard any indirect coupling caused by the

reflection or scattering of other-channel emission throughout the room in this case. While such multiple-bounce paths are a concern in spatially-multiplexed VLC systems, they are difficult to model due to their reliance on the layout of walls and objects in a room.

IV. Prototype

We designed and prototyped a VLC bulb to illuminate a 60degree FOV for covering 2×2m on the work surface in the room from a height of 2 meters while providing optical downlinks. The bulb is intended for use along with conventional Wi-Fi, where Wi-Fi provides uplink and the bulb augments Wi-Fi with additional downlink bandwidth. This architecture provides the additional bandwidth where it is most needed as the downlink data volume is typically significantly larger than uplink. It also provides a simple architecture where remote transceivers (i.e., end-user devices or clients) can utilize the optical downlink with a simple omni-directional receiver and don't need hardware for an optical uplink. Such a hybrid (optical + RF) solution also simplifies the process of establishing and maintaining the optical link because there is a single directional component (the optical downlink) while the omni-directional RF link can be used to facilitate link initialization and maintenance [32].

A. Bulb Design: Dome Lens, LED Array, and Driver Circuitry

The bulb design focuses on Tx beams' coverage of the room as well as illumination uniformity. The Tx is made of an array of 5×5 individually addressable emitters consisting of commercially available white phosphorus LEDs with an emissive area of 25mm^2. Each LED (model: GW P9LT32.EM-PTPU-XX51-1) is actually comprised of ten individual pump emitters potted inside a phosphor-doped polymer housing. These sub-LEDs cannot be driven independently but are visible in the projected illumination pattern when the Tx plane is precisely at the front focal plane of the lens. All 25 LEDs are soldered onto a 4-layer PCB board with a 5.73mm pitch, which leaves ≈0.73 mm of dark space between the ≈5mm wide emissive regions of adjacent LEDs. We designed a printed circuit board (PCB) for the 25-LED array and soldered small solid state relays on the backside of the PCB to switch each LED between DC mode (illuminating but not transmitting) and AC mode (illuminating while transmitting). Each LED can provide a luminous flux up to 710lm at 750mA drive current. In theory, the 25-LED bulb provides a maximum flux of 17,750 lumens or an equivalent of roughly eleven standard 100W light bulbs [33]. However, driving all LEDs at full power creates an uncomfortable amount of light at standard ceiling heights and we start to observe excess heating on the PCB. For all testing reported here, we reduce the drive current to 50mA at 5.45V which yields a total luminous flux of 106 lumens comparable to a standard 60W [≈10W] bulb.

A schematic of the Tx and photo of the assembled prototype are shown in Figs. 2(a) and (b), respectively. We used a DC power supply (model: TENMA 72-6851) to drive all LEDs in DC mode and switched up to two LEDs at a time into AC mode where they were driven by an FPGA (model: SPARTAN 3E) capable of providing two simultaneous data streams at rates up to 20 MHz. Switching was performed manually by moving jumper cables between header pins on the PCB to switch the relay control signal from ground to 5VDC. In principle, this could be easily automated using the same microcontroller that would be used in a full system to instantiate, maintain and drop links as clients move through the bulb's FOV. The PCB design included 4 clearance holes to fit onto a 100 mm optical rail standard to facilitate alignment of the PCB with the lens assembly.

The lens design utilizes three off-the-shelf, uncoated, plano-convex lenses with 75mm diameter. The prescription and first-order characteristics are provided in Table I. Design optimization was conducted in ZEMAX to yield a wide FOV with minimal vignetting of the peripheral LEDs and short track length rather than minimizing aberrations. We considered our bulb tolerant to fairly large optical aberrations because we anticipated using optical blur to fill-in illumination gaps to improve uniformity. The effective focal length (EFL) is 44.56mm, half FOV is 42°, F/# is 0.57, total track length is 68mm, the front focal length (FFL) is 10mm, and the magnification is $M = 43$. At prime focus, vignetting is <2% from the top/bottom LEDs and <3.5% from the extreme diagonal LEDs. Vignetting is calculated as the fraction of lost rays emitted within the axial acceptance cone (for the corner LED with x=y=16.5mm, it was 33)(≈30°) and averaged over the emissive area of the respective LEDs.

The three lens elements were mounted in a 2" total track (i.e., depth) and 3" diameter lens tube using retaining rings. The retaining rings reduce the clear aperture diameter of the lenses by ≈1mm. This was not included in the optical model but its impact is expected to be minor. Elements were positioned manually using a graduated spanner wrench without optical feedback and this typically results in a placement accuracy of ≈100μm. The lens assembly was affixed into a cage-mount tube holder (CTH, model: SM3L10,SM3L5,SM3T1) and four optical rails were used to adjust the spacing between the lens and the PCB. An opaque black cloth was used as a baffle to minimize light leakage (i.e., bypassing the lens) into the room but this remains the most significant source of background illumination. The PCB was epoxied directly to rails after assembly and then the rails were slid through CTH to adjust distance between the PCB and the lens mount. The alignment error between the PCB normal and the cage axis is expected to be <0.5°. Five different PCB distances of $z = \{0, 3, 5, 7.5, 10\}$mm from prime focus were investigated corresponding to different defocus conditions of 0%, 6.6%, 11.1%, 16.7% and 22%, respectively. The defocus amount was oriented to increase the track length in order to maintain a real image projection but this reduced coupling efficiency with increasing defocus.

B. Experimental Measurements

The simultaneous irradiance patterns (i.e., maps) of all 25 LEDs were measured in DC mode by projecting the bulb emission horizontally onto a white projector screen. Horizontal measurements were conducted to characterize the bulb for

convenience despite the intended ceiling-mount configuration. As shown in Fig. 3, the bulb was mounted with its axis parallel to and $\approx 1m$ above the lab floor. The screen was positioned 2m away from the bulb and perpendicular to its optical axis. Ambient room lights were minimized during all experimental characterizations. Irradiance patterns were recorded by taking a high-resolution photo of the illuminated screen using a camera (Sony $\alpha 6,000$ with a 16-50mm, F/3.5-F/5.6 lens) positioned at approximately the same location as the bulb - separated by a few inches due to the physical size of the two systems. Grayscale images were taken using the camera's native color-to-grayscale conversion, which we expect to be accurate given the spectral uniformity of the bulb. Spatial sampling of the screen irradiance is $\approx 48\mu$m and the camera exposure was set so that the peak irradiance fills the camera's 12-bit depth to $\approx 60\%$ to avoid saturating the image. The camera settings were fixed to F/# =3.5, shutter speed of 1/250 seconds, and sensitivity of 2,500 ISO throughout the measurements. The image data were normalized to pixel values spanning 0 to 1, where 1 corresponds to the maximum intensity of the central LED. These patterns were used to evaluate lighting uniformity.

Individual irradiance maps were measured using the same setup described above but turning one LED on at a time. Each map was normalized to its peak value and these patterns were used to evaluate crosstalk and SINR. Semi-experimental SINR maps were generated using these irradiance patterns via Eqs. (6)-(7) while neglecting receiver noise and assuming that all 25 channels are utilized for communications, i.e., $\Lambda_{i,j} = 1$ for all LEDs. We calculate "Peak SINR" (P-SINR) using irradiance maps assuming a receiver located in the center of the beam emitted from the central LED on the array. This is a convenient reference to compare the impact of defocus; however, note that the real maximum in SINR occurs near the extreme corners where the signal is smaller than the central beam but the interference is even smaller since the other transmitting LED is located at the other corner. Also recognize that the P-SINR is a near-worst-case scenario in which all LEDs are assumed to be actively communicating.

A lux-meter (model: AMPROBE LM-100) was used to measure the peak illuminance on the screen by positioning its aperture in the center of the central LED. Measurements were made at each defocus condition to account for variations in outcoupling efficiency with varying defocus. Prior to use, the lux-meter was calibrated to convert the LED spectral content directly into lumens. This measurement allows a photometric conversion between camera-based irradiance maps generated above and illuminance maps; alternatively, converting lux-meter measurements into watts and dividing by the lux-meter aperture provides conversion from normalized irradiance maps into absolute irradiance maps.

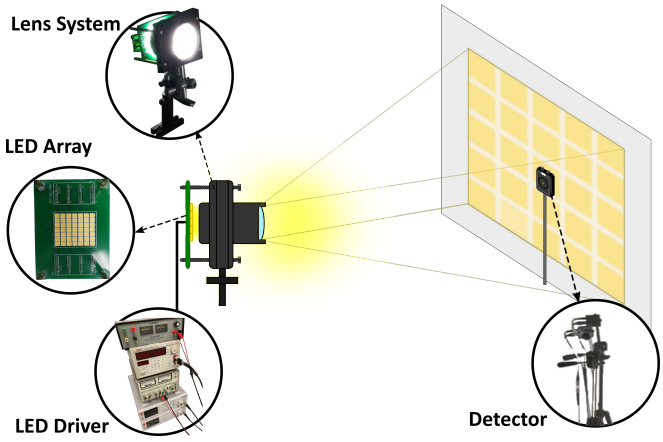

Fig. 3. The system configuration for measurements

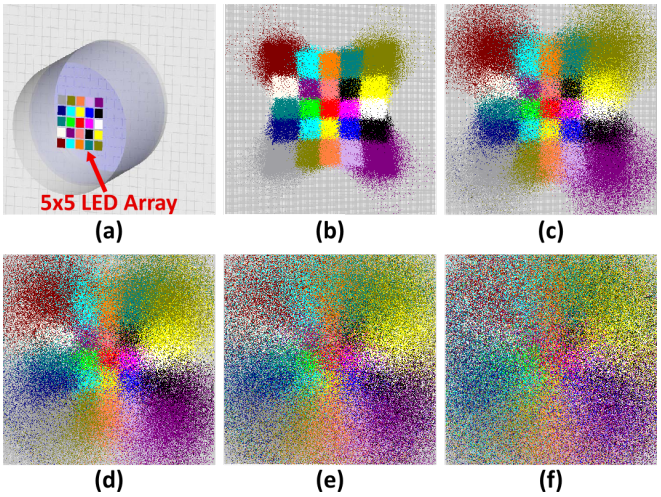

Fig. 4. Coverage Regions corresponding to each transmitter; (a) LED Array (b) Prime focus, i.e., 0% defocus, (c) 6.6%, (d) 11.1%, (e) 16.7%, (f) 22.2% defocusing percentages.

P-SINR was measured using a high-speed photodetector (model:PDA36A) positioned at the screen and centered in the emission from the central LED. An F/1.53 lens with EFL of 35mm was used to collect irradiance from a 1" diameter region on the photodiode. The signal was generated by driving the central LED with a 2MHz squarewave (i.e., 50% duty cycle). Interference from a single competing channel was measured by turning the central LED off, modulating the competing LED, and recording the average power coupled into the photodiode. Total interference is calculated using Eq. (7) by summing contributions from all 24 competing LEDs. The experimental P-SINR is taken as the ratio of the received signal power to the total interference power.

V. Results

We performed several measurements from the prototype and compared them to a simulation model.

Optical irradiance simulations were conducted using FRED Optical Engineering Software [34], [35]. Each LED is simulated as a uniform $5\times5\text{mm}^2$ emissive area with Lambertian angular distribution and spectrum that matches the LED datasheet. Emission from all 25 LEDs was simulated using 5×10^9 rays from each LED to generate color-coded irradiance maps from the simulations. Subsequently, optical simulations were refined to capture the sub-LED structure observed near prime focus. Here, the ten sub-LEDs (of an LED) were

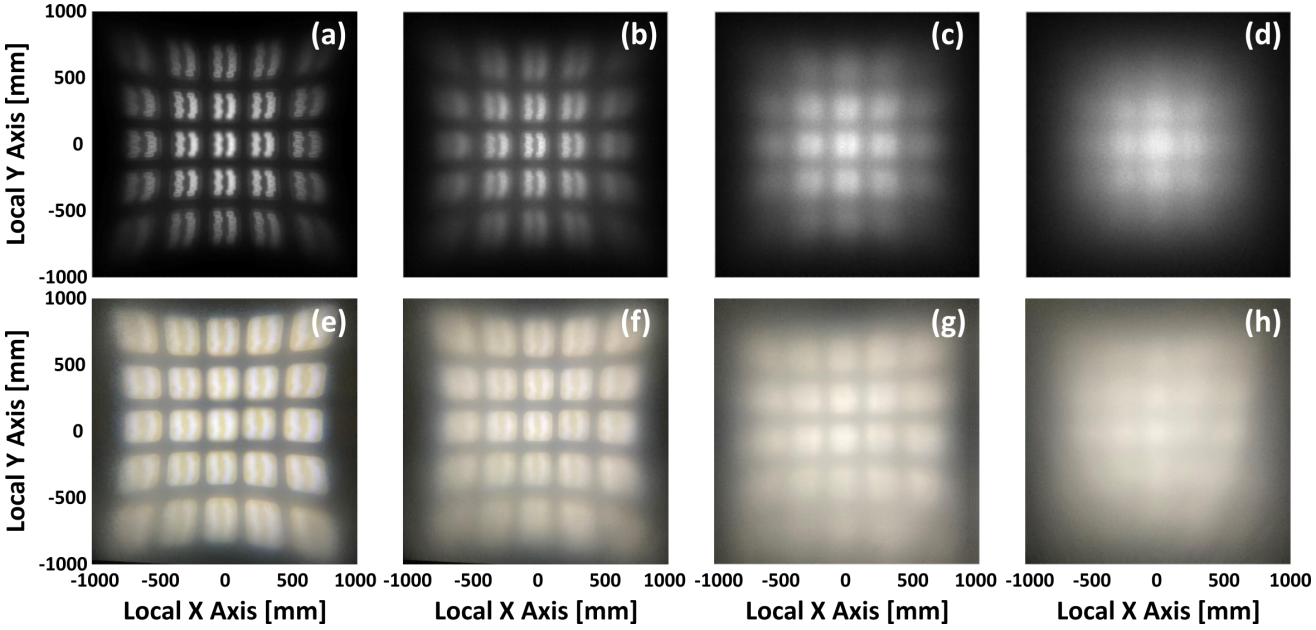

Fig. 5. Simulated illumination profile at (a) 6.6%, (b) 11.1%, (c) 16.7%, and (d) 22.2% defocusing percentages. Experimental illumination profile at (e) 6.6%, (f) 11.1%, (g) 16.7%, and (h) 22.2% defocusing percentages.

simulated and arranged into the pattern indicated in the LED datasheet. Simulated irradiance maps are compared with measured results including both qualitative spatial patterns and P-SINR.

A. Impact of Defocus on Lighting Uniformity

Raytracing results from FRED simulations under the five defocus conditions are provided in Fig. 4. LEDs are modeled as uniform (square) intensity sources without sub-LED structure to illustrate the imaging relay provided by the optics. Rays are traced from the different parts of each LED, through the lens assembly, and to a flat surface located 2m from the lens. Rays from each of the 25 LEDs are color-coded according to the LED source layout illustrated in part (a). Parts (b)-(f) show the relative confinement and mixing associated with different defocus conditions, respectively, corresponding to: 0, 3, 5, 7.5, and 10mm of defocus.

Fig. 5(a-d) shows the results of the FRED modeling including the ten sub-LEDs comprising a single LED source. Here emission from all LED sources are summed to generate irradiance maps showing the cumulative irradiance projected onto a screen 2m away from the lens. In all images, the gray scale is normalized from 0 to 1, where 0 represents no light and 1 represents peak irradiance in the image. The x and y scale on all images covers the same 2m$\times$2m region. Parts (e-h) show photos of the projected irradiance pattern in the experimental setup. Parts (a) and (e) show the modeled and experimental irradiance maps for a 6.6% defocus, parts (b) and (f) show for 11.1% defocus, parts (c) and (g) show for 16.7% defocus, and parts (d) and (h) show for 22.2% defocus. The agreement between the model and the experiment is very good, but there are small differences. The experiment exhibits secondary scattering from the LED package and lens surfaces, evidenced by additional illumination in the non-emissive space between LEDs and in each LED square surrounding the sub-LEDs. The model accounts for optical blur but not these multipath effects. This scattering actually improves illumination uniformity at the expense of channel isolation. Both model and experiment show the irradiance pattern becomes more uniform as the defocus is increased leveraging the optical blur to mix the spatially independent channels. Section VI discusses the trade-offs between uniformity and isolation for this system in more detail.

Fig. 6(a) shows the power distribution cross-section of the simulated and experimental results. Cross-sections were obtained from Fig. 5 images by performing a vertical average of 15 consecutive rows cutting across the center of each respective image near $y = 0$mm, which results in a smoothed representation of the $y = 0$mm data. The simulation results are not normalized because photometrically accurate models were used for the LEDs as described in Section IV. However, the experimental data was normalized for each defocus according to the illuminance measured independently using a lux-meter positioned at the center of the bulb's illumination. This normalization accounts for the unknown conversion from radiant flux to digital levels in the camera imagery. In Fig. 6(a), five obvious peaks are easily recognizable for 6.6% (black) and 11.1% (red) defocus due to the distinct dim regions associated with non-emissive areas on the LED source array. As the defocus increases, these peaks and dips disappear since increasing blur leads to a more uniform intensity profile. Good agreement between the simulation and the experiment is evident through the close alignment of the peaks and dips. While increasing the defocus smooths the illumination pattern, the total luminous flux drops as the Lambertian LED emission is coupled less efficiently through the lens. As the working distance increases with defocus, less light is coupled to the entrance pupil of the lens as the angle α in Eq. (3) decreases according to

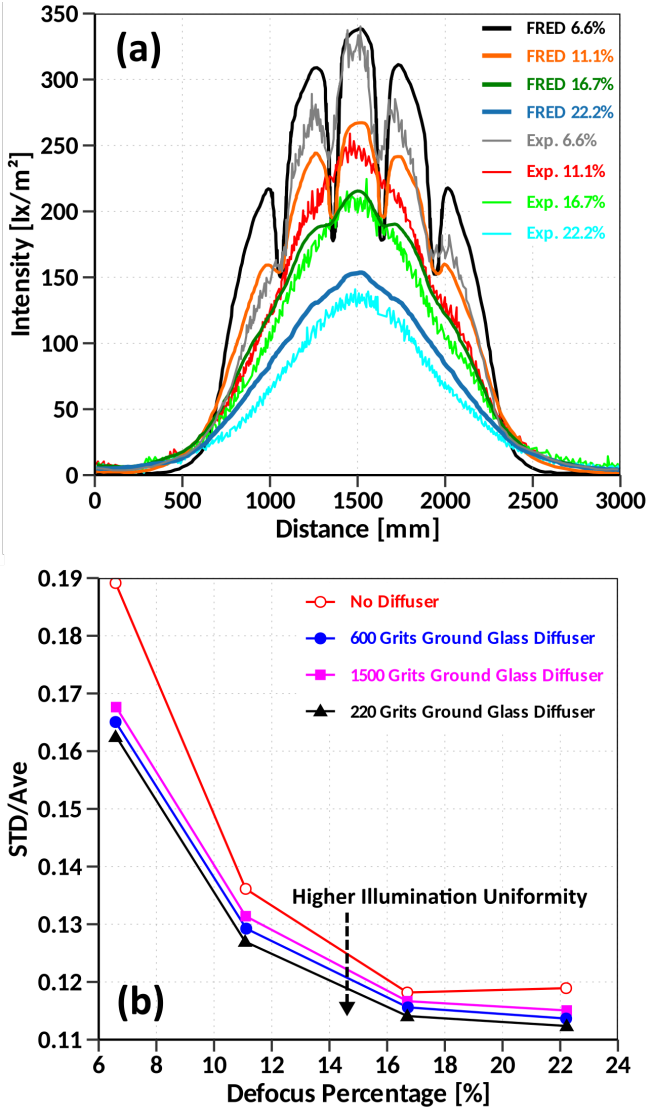

Fig. 6. (a) Intensity profile at $y = 0$ as a function of defocus percentage. (b) Illumination uniformity, U, from Eq. (4) for various defocus conditions.

$\alpha = \tan^{-1}(D/2(f + \Delta z))$. The observed reduction in power agrees well with the model where the coupling efficiency is 62% at the prime focus and drops to 51% at $\Delta z = 10$mm. The illumination uniformity is shown in (b) for a 2m×2m square region and centered at x=y=0; the uniformity is evaluated according to Eq. (4) as the ratio of the standard deviation normalized by the average illuminance (STD/Ave). The impact of defocus on uniformity is masked by the roughly Gaussian envelope of the illuminance pattern, whereas the uniformity of a nominally flat-top illuminance pattern would be more sensitive to the pronounced dark regions observed at small defocus.

B. Impact of Defocus on SNR and SINR

An additional set of 25 irradiance maps were measured using the same configuration as in Fig. 5 except that only one LED was turned on at a time to obtain the distribution of irradiance from all 25 LEDs as projected onto a screen at a distance of 2m, including optical blur and multipath effects. This data was collected to calculate high-resolution interference maps. An example SINR map for four defocus cases is shown in Fig. 7(a)-(d). Here, all 25 LED sources are considered to be transmitting data utilizing the full capacity of the bulb's 25 data channels because this provides a worst case scenario for SINR. In general, all channels would rarely be utilized at once and the SINR will generally be higher than shown. The SINR maps are generated by considering the origin of all irradiance arriving at each location in the illuminated area. Signal irradiance comes from the single LED that provides the most light at a given location - this LED is designated to cover this location in the room. Interfering irradiance is the sum of all contributions at that location from all 24 other LEDs. Of course, the most significant contributions to interference come from the immediately adjacent LEDs while more distant LEDs contribute less. Likewise, with even the smallest defocus, interference dominates the receiver noise. The low SINR transitions between zones are affected by defocus-induced blur but cannot be eliminated in this prototype; eliminating dead-space in the transmitter array and operating at prime focus is the most effective way to reduce the footprint of the low SINR regions. Here, we want a small amount of defocus as in (a) or (b) to retain sufficient SINR to maintain channel link integrity; however, this results in reduced lighting uniformity than we get with larger defocus as in (c) or (d). We consider the 11.1% defocus as an optimal balance for signal integrity and uniformity when all channels are allowed to operate simultaneously. In Section VI, we discuss alternative protocols to increase SINR or allow more blur to achieve greater uniformity at the expense of bandwidth. The peak SINR values in the maps lie at the distal corners of the map, which exhibit relatively low irradiance overall. This arises due to reduced interference because there are fewer adjacent LEDs contributing irradiance to these regions. If additional bulbs were used to provide additional VLC lighting

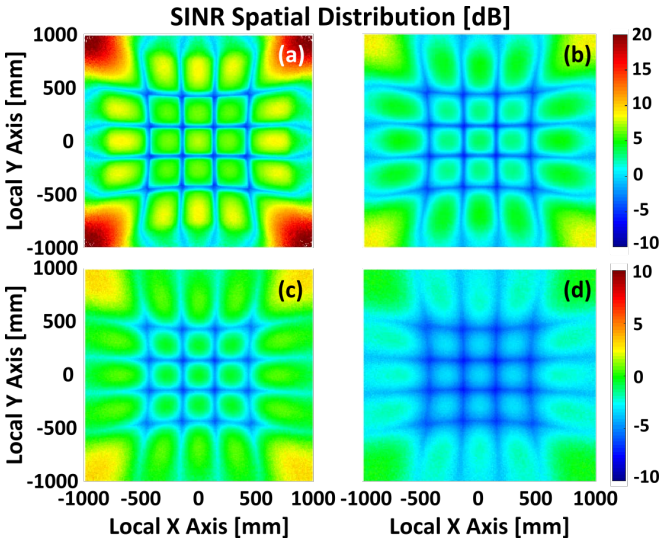

Fig. 7. SINR map for (a) 6.6%, (b) 11.1%, (c) 16.7%, and (d) 22.2% defocusing percentages. The top color bar applies to (a) and (b) while the bottom applies to (c) and (d).

over a larger room area, they would likely be spaced on a 2m grid with some overlap in illumination around the border, and this may reduce these peak SINR values at the extremities.

Fig. 8 shows the SNR and SINR at the center of the bulb illumination pattern as a function of defocus. SINR is calculated from the FRED simulations shown in Fig. 5 (a-d) and compared with two experimental measurements. SNR values drop the interference contributions in Eq. (6) and reflect the maximum SINR generated if only one channel is used at a time. The SINR curves represent the maximum interference with all channels in use at full capacity. In general, communication protocol designs to manage interference would boost SINR toward the SNR curves. Both experimental methods use a receiver positioned at the center of the bulb illumination pattern. Method 1 is a time-domain measurement using the mixed (i.e., beat) signal generated by two LEDs (the central LED and one adjacent LED) modulated at slightly different frequencies while all other LEDs are on for illumination but not transmitting. Separate measurements were made for both the nearest-neighbor (NN) and nearest-diagonal-neighbor (NDN) while interference contributions from more distant LEDs are considered negligible. The interference power extracted from these two-channel measurements were scaled four times to capture the degradation from all 4 NNs (left, right, up, and down) and all 4 NDNs (up-left, up-right, down-left, down-right). Method 2 measures the power on a receiver positioned at the center of the bulb illumination pattern. The received power is measured for each LED one by one (all other LEDs turned off) and these measurements are summed according to Eqs. (6) and (7). The inset shows the power contributions of all 25 LEDs for a receiver centered in the illumination pattern according to method 2 with a defocus of 11.1%. As expected, there is clear isolation between the channels and the most significant interference comes from nearest neighbors. Overall, there is excellent agreement between the model results and both experimental measurements - the largest departure is on method 1 measurements at large defocus where the beat signal is weakest resulting in the largest errors extracting the relative power amplitudes from the two modulated sources.

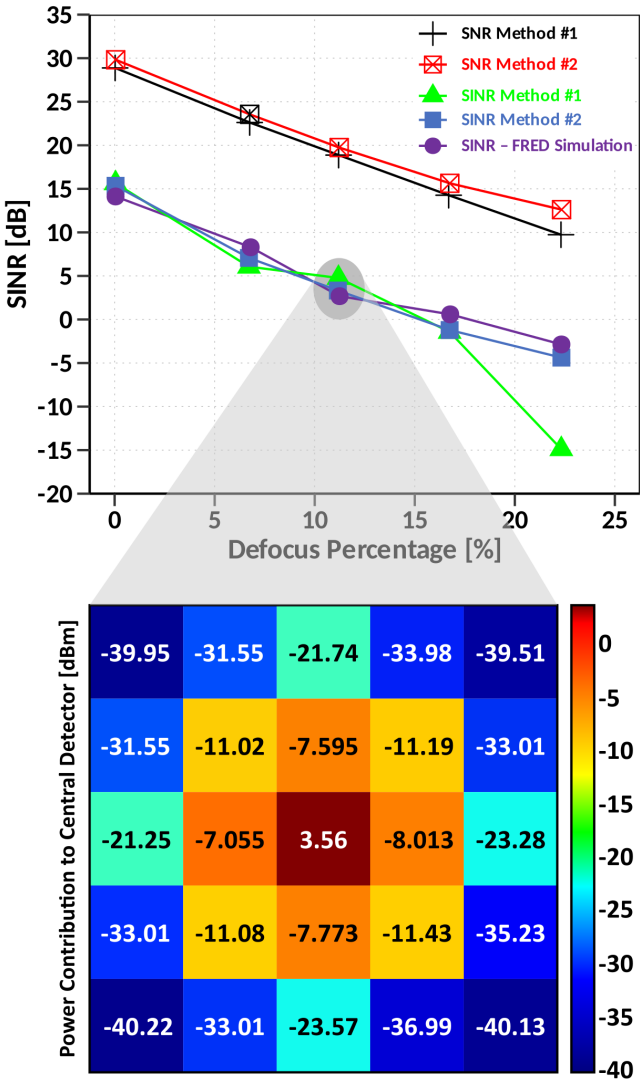

Fig. 8. Signal-to-noise ratio (SNR) and SINR as a function of defocus for a receiver centered in the bulb illumination pattern. Method 1 utilizes the beat amplitudes from adjacent LEDs driven at different frequencies; method 2 uses DC measurement of power received from each LED. Both are combined using Eqs. (6) and (7) to compute SINR while SNR is computed without considering interference from other LEDs. Inset: power contributed from each LED to a 1cm diameter receiver positioned at the center of the bulb emission with 11.1% defocus. Scale bar and text values are in dBm.

C. Impact of a Diffuser at the Focal Plane

Next, we consider the effect of utilizing a diffuser to modify the irradiance profile of the LED array in an attempt to further increase the illumination uniformity and SINR. We positioned a diffuser at the lens focal plane while the LED array was defocused away from the lens; in this configuration, the LED array illuminates the diffuser positioned at prime focus, and the diffused light was relayed by the lens to illuminate the room. The LED emission expands over a short distance to the diffuser filling in some of the dark (i.e., non-emissive) regions across the LED array, the diffuser scatters this light and the lens projects the image of the diffuser at prime focus. We evaluated this configuration using ground glass diffusers from Edmund Optics with grits of 220, 600 and 1500 lines per inch. We modeled the diffuser in FRED as a square plate (100mm $\times$ 100mm) made of N-BK7 with a thickness of 1.6 mm. Intensity profiles for the diffusers were translated to Harvey-Shack normalized Bi-Directional Transmittance Distribution Function (BTDF) models for use in FRED. A finer grit (such as 1500) results in a smaller diffuser pattern, whereas a coarser grit (such as 220) results in a larger diffuser pattern. As illustrated in Fig. 6(b), ground glass diffusers polished to a coarser grit have the ability to increase lighting uniformity while also modestly increasing SINR (0.5 dB). Utilizing such diffusers will also aid in smoothing out the illumination inconsistency generated by each LED's integrated smaller LED chips. Fig. 9 simulates the effect of a 220-grit diffuser deployed at the focal plane on the irradiance pattern produced by the bulb; corresponding patterns without the diffuser are reproduced for comparison. The experimental results follow the model results shown, which were used for quantitative analysis. As expected, the diffuser increased the uniformity

TABLE II
PARAMETERS FOR RECEIVER AND NOISE MODELING

Coefficient	Value
Receiver Aperture Area	$1\ \mathrm{cm}^2$
Responsivity, $\mathcal{R}$	$0.8\mathrm{A/W}$
Max electronic bandwidth, B	$20\ \mathrm{MHz}$
Optical bandwidth	$350 - 1100\ \mathrm{nm}$
Equivalent temperature, T_e	$300\ \mathrm{K}$
Thermal Noise, P_{noise}	$5.15 \times 10^{-15}\ \mathrm{W}$
Load resistance, R_L	$1\ k\Omega$
Dark current, I_{dc}	$1.226 \times 10^{-9}\ \mathrm{A}$

of the illumination pattern by smoothing out the sub-pixels embedded within each individual LED and partially filling in the dark regions between LEDs. However, the improvement in SINR and uniformity was minor and it was not worth introducing an additional component and optical loss into the basic bulb design.

D. The Impact of Noise

Noise is a key parameter in VLC link budgets. Noise sources are comprised of: 1) interference from other VLC channels, 2) Johnson (i.e., thermal) noise intrinsic to the receiver, and 3) shot noise due to detector dark- and photo-currents. Intrinsic detector noises (Johnson and dark current shot noise) are expected to be small in the bright and noisy indoor environment. We adopt a simple model and consider irradiance from other VLC channels to directly add to receiver noise because these modulated signals degrade visibility of the desired signal; this "interference" is expected to be the dominant noise in dense, spatially-multiplexed VLC systems. Steady-state irradiance from ambient sources including constant (i.e., unmodulated) indoor illumination and sunlight present a constant photocurrent (J_{BG}) that is readily filtered in receiver circuitry; the shot-noise power from this photocurrent has a standard deviation of $\sigma_{BG}^2 = 2qBJ_{BG}R_L$. To consider the impact of this noise, we compare the steady-state (i.e., background) irradiance (I_{BG}) needed to yield shot-noise comparable to a typical NN interference; while NN interference depends on the location of the end-point receiver within the bulb's illumination pattern (c.f. Fig. 5) we take a nominal value of 158 μW corresponding to the NN interference into a 1 cm diameter receiver centered in the bulb illumination (i.e., centered in emission from the central LED) according to the inset of Fig. 8.

The amount of background irradiance allowed before shot-noise from that source is comparable to NN interference is found by setting $\sigma_{BG}^2(I_{BG}) = 158\mu W$ and inverting to find $I_{BG} = 3.09 \times 10^4\ W/cm^2$ or roughly 30,000 times larger than solar irradiance on a sunny day. This supports the conclusion that noise is dominated by interference associated with channel crosstalk. In Table II, we have compiled a list of important system parameters which we use to characterize the SINR.

VI. INTEGRATION TO VLC SYSTEMS

The preceding sections introduced a novel VLC transmitter that provides N=25 spatially-separated channels using non-mechanical IBBS. Each channel can operate simultaneously, increasing the system throughput by a factor of N times the channel bandwidth. Integration of this design into dense VLC networks opens new opportunities, but also brings challenges, some of which we discuss next.

A. Mobility and Handover

Recognizing new end-point users within the FOV, allocating VLC channels to them, and tracking to maintain the VLC link present new challenges for spatially-multiplexed VLC systems. This is necessary to have efficient hand-over (HO) mechanisms in place to establish and maintain a connection while the user is moving between projected light spots. Our dome bulb design can be used to facilitate various HO mechanisms depending on what capabilities the receivers have. In a hybrid VLC network where receivers can use a Wi-Fi uplink to a controller in the bulb, our dome bulb design can utilize a horizontal HO [16], [36] method to handle mobile users. In this method, the bulb periodically transmits SEARCH frames via its transmitter LEDs to conduct a search for new receivers in the room. Each LED in the array has a unique local identifier, k, transmitted in the SEARCH frames. These SEARCH frames are similar to Ethernet request-to-send (RTS) messages, except that the LED's local ID is included. As a mobile user X enters the room, these SEARCH frames are received. After receiving the SEARCH frame from LED k, the user transmits an acknowledgment (ACK) frame via its Wi-Fi transmitter (similar to a clear-to-send, CTS, frame in Ethernet) to the controller in the bulb. This ACK contains the Ethernet/medium access control (MAC) address of the user, as well as the local ID of the LED from which the SEARCH frame was received, k. The ACK signal indicates to the bulb that user X is at the spot that is illuminated by the LED k, which means that the controller can steer the data packets destined for user X to LED k on the array. As the user moves around in the room, it will be associated with its corresponding LED in the array using this SEARCH-ACK HO protocol.

Our bulb design uses defocusing to increase the uniformity of the lighting in the room. Increased defocusing improves lighting in the room and eliminates spotty lighting on the floor, which is an important goal of LiFi networks, but at the cost of crosstalk interference from adjacent cells and a decrease in the receiver's HO protocol's efficiency. The increased defocusing will cause the user X to receive multiple LED IDs, from the primary transmitting LED and also from adjacent LEDs that leak optical power to the user due to the LED array's interference and defocusing. The receiver can filter out the highest-intensity SEARCH frame by measuring the received signal strength indication (RSSI); however, the defocusing will make it more difficult for the receiver to use the maximize RSSI method to determine the local ID of its intended transmitting LED. The inset of Fig. 8 illustrates that interference is dominated by the nearest (NN) and nearest diagonal (NDN) neighbor emission while more distant LEDs contribute negligible interference. The receiver can use this information to improve its HO algorithm, enabling it to identify the transmitting LED's local ID more efficiently when multiple streams are received as a result of defocusing-induced interference.

B. Receivers and Uplink

Design of a proper receiver at the mobile user and integration of uplink from the user to bulb present new technical challenges. To establish optical uplinks to the overhead bulb, end-point devices (i.e., users) must have an optical receiver and transmitter with a clear LOS to the bulb. Optical uplinks would require an optical receiving path via an adjacent aperture or sharing the same aperture. In principle, the LED array and driver circuitry in the transmitter could be replaced with a photodiode array and detector circuitry to make a matched receiver that uses the same spatial filtering through IBBS to provide N independent bi-directional optical channels out of a single bulb. However, the optical uplink path has very different requirements (e.g. does not need to provide illumination and can operate using infrared spectrum), so that an optimized receiver may look very different from the transmitter.

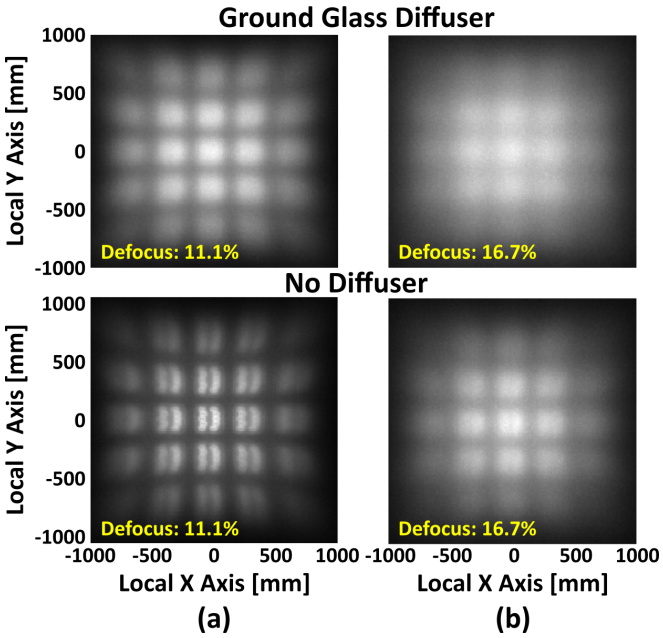

Fig. 9. Improvement obtained at various defocusing percentages when a 220 Grits Ground Glass Diffuser was used at the focal plane.;(a) 11.1%, (b) 16.7% defocusing percentages.

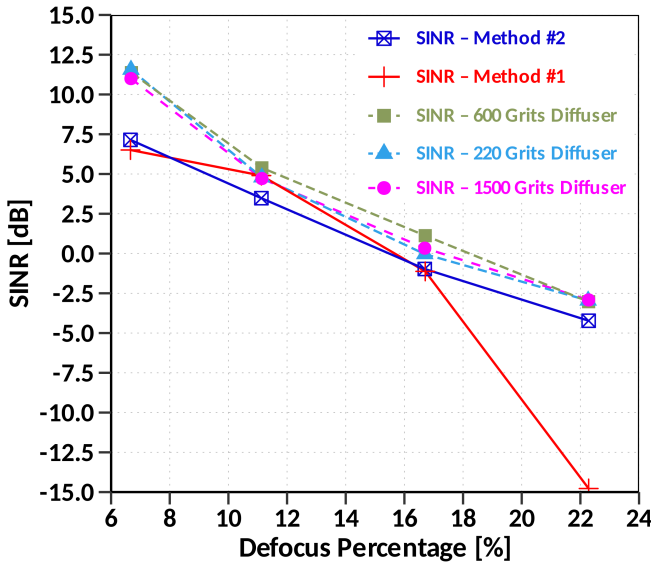

Fig. 10. SINR Improvement when a Ground Glass Diffuser was used at the focal plane.

Mobile devices may use simple, omni-directional receivers and transmitters without active steering. End-points could utilize a simple omni-directional photodiode receiver that could be integrated into smart devices or added using an external device [37]. For example, in [26], the downlink (visible) and uplink (infrared) paths were spectrally isolated to mitigate potential crosstalk concerns between end-point devices. However, multi-path interference is still a concern with omni-directional receivers. If one end-point sends light to another part of the room and that light is reflected toward the overhead bulb, this will contribute interference to the channel addressing that part of the room. In contrast, a hybrid approach could mitigate the multi-path uplink concerns by replacing the optical uplink with an RF uplink. Of course, the uplink path loses the benefits of wireless optical connectivity, including increased bandwidth and tight spatial reuse of the spectrum. This may be acceptable for end-user access points, which tend to have significantly larger downlink utilization than uplink. Additionally, the bulb transmitter could employ an RF downlink as a backup if the LOS to the bulb is interrupted [38], [39]. The transmitter design we introduce here could support both architectures of the system.

VII. Conclusion and Future Work

We designed and prototyped a VLC bulb that employs IBBS to passively steer emission from $N = 25$ LEDs to unique regions of the room. This architecture allows simultaneous data transmission on all 25 LED channels to increase downlink capacity by a factor of 25 beyond the bandwidth of an individual LED; LED bandwidth was limited to 20 Mbps while this bulb could provide up to 500 Mbps throughput. We conducted detailed modeling and compared against experiment to analyze the lighting uniformity and link SINR. The results showed that defocus provides a simple mechanism to trade between uniformity and SINR. We discussed that interference due to crosstalk dominates other noise sources and identified mitigation strategies to move from the worst-case SINR reported (i.e., full crosstalk) toward the best-case when there is no interference. We also discussed additional methods to improve uniformity. This architecture provides a novel platform for VLC implementation with unique degrees of freedom to improve performance for dense environments. More generally, the spatial reuse and simultaneous multiplexing enabled by IBBS could find application in optical wireless and free-space optical communication systems beyond the VLC.

For simplicity, we drove all the LEDs at the same bias level during this work. This led to a gradual reduction in the envelope irradiance from the center of the illumination pattern toward the edge. The uniformity could be improved by simply driving the LEDs with different biases according to their location in the array. There are two features to compensate for: 1) optical blur and 2) vignetting. Optical blur increases

toward the edge so that the emission from edge LEDs is spread out more, lowering the irradiance they contribute. This is exacerbated at the edge of the array by fewer nearest neighbors and nearest diagonal neighbors to contribute spill-over irradiance to edge LED zones. Vignetting is caused by inefficient coupling through the lens apertures toward the edges of the array. As noted before, the LEDs could be driven at much higher powers given better thermal management (e.g. using higher temperature solder, and heat sink) so there is room to boost power toward the edge of the array and increase uniformity.

Furthermore, we neglected to account for the SINR degradation caused by optical multi-path effects which arise from indirect (i.e., non-LOS) routes between Tx and Rx. Reflections from walls, floor and other objects in the room can cause signals to propagate from the bulb to end-point receivers over multiple paths; these are usually diffuse reflections that can be described via a Lambertian radiation model. [40], [41] Multipath propagation of optical signals introduces time dispersion that can generate inter-symbol interference (ISI); two bounces around a 3m wide room to traverse an additional 6m of path induces 20 ns of delay or 40% of the bit rate in a 20 MHz system. In [40], R. Raj *et al.* describe a multipath channel model and its detrimental effects for indoor VLC systems. Efficient equalization techniques, such as Multiple Symbol Detection algorithms, can be used to mitigate ISI [26].

Finally, the cost and size of our design can be optimized for the room that it will serve. We utilized 25 LEDs arranged in a planar 5×5 grid to illuminate a small office area of $4m^2$ with a covering angle for 60×60 degrees. It may be possible to attain the illumination and communication goals with an array of fewer LEDs. Likewise, the size of the dome-shaped lens (which was the total track (depth) of 2" and 3" diameter lenses in our prototype) can be further optimized for the dimensions of the room.

REFERENCES

[1] T. Koonen, K. A. Mekonnen, F. Huijskens, N.-Q. Pham, Z. Cao, and E. Tangdiongga, "Fully passive user localization for beam-steered high-capacity optical wireless communication system," *Journal of Lightwave Technology*, vol. 38, no. 10, pp. 2842–2848, 2020.

[2] H. Haas, L. Yin, Y. Wang, and C. Chen, "What is LiFi?" *Journal of lightwave technology*, vol. 34, no. 6, pp. 1533–1544, 2016.

[3] Y. Wang, Y. Wang, N. Chi, J. Yu, and H. Shang, "Demonstration of 575-mb/s downlink and 225-mb/s uplink bi-directional scm-wdm visible light communication using rgb led and phosphor-based led," *Optics express*, vol. 21, no. 1, pp. 1203–1208, 2013.

[4] X. Meng, L. Wang, Z. Hao, Y.Luo, S. Cand Han Y, B. Xiong, J. Wang, and H.Li, "Study on efficiency droop in InGaN/GaN light-emitting diodes based on differential carrier lifetime analysis." *Applied Physics Letters*, Jan 2016.

[5] R. Olshansky, C. Su, J. Manning, and W. Powazinik, "Measurement of radiative and nonradiative recombination rates in InGaAsP and AlGaAs light sources," *IEEE Journal of Quantum Electronics*, vol. 20, no. 8, pp. 838–854, August 1984.

[6] C. Du, X. Huang, C. Jiang, X. Pu, Z. Zhao, L. Jing, W. Hu, and Z. Lin Wang, "Tuning carrier lifetime in InGaN/GaN LEDs via strain compensation for high-speed visible light communication." *Scientific reports.*, Nov 2016.

[7] G. M. David A, "Influence of polarization fields on carrier lifetime and recombination rates in ingan-based light-emitting diodes." *Applied Physics Letters*, vol. 97, July 2010.

[8] G. P. Agrawal, *Fiber-optic communication systems*. John Wiley & Sons, 2012, vol. 222.

[9] S. Park, D. Jung, H. Shin, D. Shin, Y. Hyun, K. Lee, and Y. Oh, "Information broadcasting system based on visible light signboard," *Proceedings of the Wireless and Optical Communications, Montreal, QC, Canada*, vol. 30, 2007.

[10] G. Cossu, A. Khalid, P. Choudhury, R. Corsini, and E. Ciaramella, "3.4 Gbit/s visible optical wireless transmission based on RGB LED," *Optics express*, vol. 20, no. 26, pp. B501–B506, 2012.

[11] J. J. Wierer Jr, J. Y. Tsao, and D. S. Sizov, "Comparison between blue lasers and light-emitting diodes for future solid-state lighting," *Laser & Photonics Reviews*, vol. 7, no. 6, pp. 963–993, 2013.

[12] S. Watson, M. Tan, S. P. Najda, P. Perlin, M. Leszczynski, G. Targowski, S. Grzanka, and A. Kelly, "Visible light communications using a directly modulated 422 nm gan laser diode," *Optics letters*, vol. 38, no. 19, pp. 3792–3794, 2013.

[13] L.-Y. Wei, C.-W. Hsu, Y. Hsu, C.-W. Chow, and C.-H. Yeh, "20 Gbit/s tricolor R/G/B laser diode based bi-directional signal remodulation visible light communication system," in *Optical Fiber Communication Conference*. Optical Society of America, 2018, pp. M3K–2.

[14] H. Alshaer and H. Haas, "Bidirectional LiFi attocell access point slicing scheme," *IEEE Transactions on Network and Service Management*, vol. 15, no. 3, pp. 909–922, 2018.

[15] S. I. Mushfique, A. Alsharoa, and M. Yuksel, "Optimization of SINR and illumination uniformity in multi-LED multi-datastream VLC networks," *IEEE Transactions on Cognitive Communications and Networking*, 2020.

[16] S. I. Mushfique, P. Palathingal, Y. S. Eroglu, M. Yuksel, I. Guvenc, and N. Pala, "A software-defined multi-element VLC architecture," *IEEE Communications Magazine*, vol. 56, no. 2, pp. 196–203, February 2018.

[17] S. S. Polkoo and C. K. Renshaw, "Imaging-based beam steering for free-space optical communication," *Applied optics*, vol. 58, no. 13, pp. D12–D21, 2019.

[18] S. Saghaye-Polkoo, P. Nabavi, M. Yuksel, and K. Renshaw, "Multi-LED multi-datastream dome bulb for dense visible light communication networks," in *Proceedings of the Workshop on Light Up the IoT*, 2020, pp. 12–17.

[19] W.-C. Wang, C.-H. Cheng, H.-Y. Wang, and G.-R. Lin, "White-light color conversion with red/green/violet laser diodes and yellow light-emitting diode mixing for 34.8 Gbit/s visible lighting communication," *Photonics Research*, vol. 8, no. 8, pp. 1398–1408, 2020.

[20] T. Little, M. Rahaim, I. Abdalla, E. Lam, R. Mcallister, and A. M. Vegni, "A multi-cell lighting testbed for VLC and VLP," in *2018 Global LIFI Congress (GLC)*, 2018, pp. 1–6.

[21] M. Toyoshima, N. Miyashita, Y. Takayama, H. Kunimori, and S. Kimura, "System analysis of non-mechanical compact optical transceiver for wireless communications with a VCSEL array," in *2008 6th International Symposium on Communication Systems, Networks and Digital Signal Processing*. IEEE, 2008, pp. 187–190.

[22] ——, "Non mechanical compact optical transceiver for wireless communications with a VCSEL array," in *Mobile and Wireless Communications Network Layer and Circuit Level Design*. IntechOpen, 2010.

[23] Y.-C. Chang, M. C. Shin, C. T. Phare, S. A. Miller, E. Shim, and M. Lipson, "2D beam steerer based on metalens on silicon photonics," *Optics Express*, vol. 29, no. 2, pp. 854–864, 2021.

[24] B. Han and S. Hranilovic, "A fixed-scale pixelated MIMO visible light communication system," *IEEE Journal on Selected Areas in Communications*, vol. 36, no. 1, pp. 203–211, 2018.

[25] R. C. Short, M. A. Cosgrove, D. L. Clark, and P. J. Oleski, "Performance of a demonstration system for simultaneous laser beacon tracking and low-data-rate optical communications with multiple platforms," in *Free-Space Laser Communication Technologies III*, vol. 1417. SPIE, 1991, pp. 464–475.

[26] P. Nabavi and M. Yuksel, "Comprehensive design and prototype of VLC receivers with large detection areas," *Journal of Lightwave Technology*, vol. 38, no. 16, pp. 4187–4204, 2020.

[27] Z. Li, S. Shao, A. Khreishah, M. Ayyash, I. Abdalla, H. Elgala, M. Rahaim, and T. Little, "Design and implementation of a hybrid RF-VLC system with bandwidth aggregation," in *2018 14th International Wireless Communications & Mobile Computing Conference (IWCMC)*. IEEE, 2018, pp. 194–200.

[28] M. E. Warren, D. Podva, P. Dacha, M. K. Block, C. J. Helms, J. Maynard, and R. F. Carson, "Low-divergence high-power VCSEL arrays for lidar application," in *Vertical-Cavity Surface-Emitting Lasers XXII*, vol. 10552. International Society for Optics and Photonics, 2018, p. 105520E.

[29] I. Moreno, "Illumination uniformity assessment based on human vision," *Optics letters*, vol. 35, no. 23, pp. 4030–4032, 2010.

[30] "ISO 8995-1:2002 Lighting of work places," https://www.iso.org/standard/28857.html.
[31] G. Einarsson, *Principles of Lightwave Communications*. New York: Wiley, 1996.
[32] A. Gupta, P. Garg, and N. Sharma, "Hybrid LiFi—WiFi indoor broadcasting system," in *2017 IEEE 28th Annual International Symposium on Personal, Indoor, and Mobile Radio Communications (PIMRC)*. IEEE, 2017, pp. 1–6.
[33] How many lumens is equivalent to a 100 watt light bulb? [Online]. Available: https://westlakehardware.com/resources/tips-tricks/how-many-lumens-is-equivalent-to-a-100-watt-light-bulb
[34] Photon Engineering, LLC., "FRED optical engineering software," https://photonengr.com/fred-software.
[35] R. G. Irvin, "Photon Engineering LLC: FRED optical engineering software by photon engineering: advancing the state of the art of optical computations," in *SPIE Exhibition Product Demonstrations*, C. Chair, Ed., vol. OP20EX, International Society for Optics and Photonics. SPIE, 2020. [Online]. Available: https://doi.org/10.1117/12.2580746
[36] A. M. Vegni and T. D. C. Little, "Handover in VLC systems with cooperating mobile devices," in *2012 International Conference on Computing, Networking and Communications (ICNC)*, 2012, pp. 126–130.
[37] Pure LiFi corporate, "chief executive scientist: Professor Harald Haas FRSE," https://purelifi.com/lifi-products/.
[38] D. A. Basnayaka and H. Haas, "Hybrid RF and VLC systems: Improving user data rate performance of VLC systems," in *2015 IEEE 81st Vehicular Technology Conference (VTC Spring)*. IEEE, 2015, pp. 1–5.
[39] M. B. Rahaim, A. M. Vegni, and T. D. Little, "A hybrid radio frequency and broadcast visible light communication system," in *2011 IEEE GLOBECOM Workshops (GC Wkshps)*. IEEE, 2011, pp. 792–796.
[40] R. Raj, S. Jaiswal, and A. Dixit, "On the effect of multipath reflections in indoor visible light communication links: Channel characterization and ber analysis," *IEEE Access*, vol. 8, pp. 190 620–190 636, 2020.
[41] ——, "Dimming-based modulation schemes for visible light communication: Spectral analysis and isi mitigation," *IEEE Open Journal of the Communications Society*, vol. 2, pp. 1777–1798, 2021.